Investigation on the Angle and Spectral Dependence of the Internal and the External Quantum Efficiency of Crystalline Silicon Solar Cells and Modules

Nils Reiners, Ulf Blieske, and Susanne Siebentritt

***Abstract*—To improve energy yield predictions and to fully understand the physical behavior of solar cells, it is necessary to investigate the effects caused by a change in the angle of incidence. All relevant angle-dependent effects are presented in this paper and angular correction factors are introduced. A new analytical model is presented, which includes internal reflection, free carrier absorption, and other parasitic absorption processes. The angular effects were exemplarily studied for the case of a very simple planar solar cell sample and a standard module sample. With an effective angle approach, the variation of the internal quantum efficiency in the standard solar module could be emulated and the results were verified with the help of a ray tracing tool developed for this purpose. The influence of the different angular factors on the current density of a standard module at an incidence angle of 70° is finally presented.**

***Index Terms*—Angle of incidence (AOI), free carrier absorption (FCA), oblique light, quantum efficiency, spectral response.**

I. Introduction

FOR the characterization of solar cells and modules in practice, the so-called standard test conditions (STC) are employed [1]. However, to calculate the energy yield of a mounted module, the incident angle needs to be taken into account because of the permanently changing position of the sun relative to the normal of the modules surface. For this purpose, the common approach is to employ an incidence angle modifier [2]–[4] to correct the current under STC to any other AOI. But recently, two papers emphasized the fact that angle dependence of the external quantum efficiency (EQE), and thus, the IAM can vary significantly depending on the wavelength of the incident light [5], [6]. While both contributions primarily concentrate on the measurement of the effect for different cell and module technologies, a systematic analysis of the underlying physical effects is still not available. Therefore, this paper presents an overview of the most relevant angular effects and gives a detailed analysis of these, using an analytical model as well as a ray tracing tool. Thereby a strong emphasis is put on the angle dependence of the internal quantum efficiency (IQE). As the generation profile inside the solar cell changes with the variation of the angle of incidence (AOI), the IQE is also influenced. Even though most researchers are aware of this effect, no systematic investigation on its extent has been presented so far.

Manuscript received February 16, 2018; revised May 21, 2018; accepted June 25, 2018. *(Corresponding author: Nils Reiners.)*

N. Reiners and U. Blieske are with the Cologne Institute for Renewable Energy, University of Applied Sciences Cologne, Cologne D-50679, Germany (e-mail: nils.reiners@posteo.de; ulf.blieske@th-koeln.de).

S. Siebentritt is with the Laboratory for Photovoltaics, Physics and Materials Science Research Unit, University of Luxembourg, Belvaux L-4422, Luxembourg (e-mail: susanne.siebentritt@uni.lu).

Color versions of one or more of the figures in this paper are available online at http://ieeexplore.ieee.org.

Digital Object Identifier 10.1109/JPHOTOV.2018.2860956

TABLE I
Effects Due to the Change of the Incidence Angle

Effect 1	Geometrical cosine loss
Effect 2	Changing reflectance at the intersection of two media
Effect 3	Changing external light trapping of pyramidal structures
Effect 4	Changing internal light trapping inside one layer
Effect 5	Changing parasitic absorption
Effect 6	Changing generation profile inside the cell

II. Angle Dependence of the Solar Cell and Module Performance

When the AOI of the solar radiation deviates from the normal, different mechanisms change the performance of the cell or module. The most important of these effects are listed in Table I.

Due to the geometrical cosine effect, the incoming light is spread over a larger area, so that the irradiance decreases by a factor of $\cos(\theta_i)$, where θ_i is the incidence angle between the normal of the cell or module and the incoming light. The cosine loss is a very pronounced effect, as can be seen by the fact that the irradiance is reduced by half at an incidence angle of 60°. Only by changing the orientation of the module relative to the sun (tracking) or by adding additional components such as mirrors can the cosine loss be reduced.

The second effect is the change of reflectance at the boundary of two materials. If an antireflective (AR) coating is applied on the top of the adjacent medium, the variation of the incidence angle not only influences the overall amplitude of the reflection, but its specific spectral performance might also be strongly affected [7]. For the calculation of the reflectance R, the absorptance A, and the transmittance T of a thin layer interface, the transfer matrix approach is used, as described in [8].

Effect 3 describes the fact that photons that are incident on a textured surface will in most cases intersect with the texture more than once. The number of intersections between the faces of the applied structures generally depends on the geometry of the textures and on the AOI. The process, which involves multiple intersections in a texture, is referred to as external light trapping here.

In contrast, effect 4 involves internal light trapping, which describes the trajectory of photons through the whole cell before they either escape or are absorbed. Here, a distinction needs to be made between the light trapping inside electrically inactive layers, such as the glass cover and the active semiconductor layer. While for the case of the inactive layers, light trapping is only preferred if the photons are subsequently led to the semiconductor layer, for the active layer, a high light trapping performance is explicitly desired because it increases the probability of long wavelength photons being absorbed in the semiconductor. This effect can be described with the help of the path length enhancement factor Z. Recently, McIntosh *et al.* described the variation of Z inside an isotextured multicrystalline silicon solar cell as a function of wavelength and AOI [9].

Effect 5: Parasitic absorption A_{Pa} refers to any mechanism in which an absorbed photon does not lead to the generation of an electron–hole pair [10]. It is composed of the absorption in all inactive module layers A_l, the absorption in the contact fingers and bus bars A_{grid}, the free carrier absorption (FCA) A_{FCA}, and the absorption in the AR coatings A_{AR}

$$A_{\mathrm{Pa}} = A_l + A_{\mathrm{grid}} + A_{\mathrm{FCA}} + A_{\mathrm{AR}}. \tag{1}$$

For the case of a solar cell without encapsulation, the variable A_l changes to A_{back} as the back contact is the only layer that causes parasitic absorption.

The electrical process described by effect 6 is due to the changing trajectory of the photons through the semiconductor with varying AOI. The path variation of the photons is translated into a modification of the generation profile. As the IQE is a function of the generation profile, it will also be influenced by the variation of the incidence angle.

III. Methodology

At first, a spectral and angular correction parameter $f_{\mathrm{EQE}}(\theta_i, \lambda)$ that contains all the physical effects to convert the EQE at one angle to its value at perpendicular incidence (EQE_0) is introduced

$$\mathrm{EQE}\left(\theta_i\right) = f_{\mathrm{EQE}}\left(\theta_i\right) \cdot \mathrm{EQE}_0. \tag{2}$$

Regarding the determination of the IQE from an EQE measurement of a solar module or cell, the most common approach is [11]

$$\mathrm{IQE}_{\mathrm{meas}} = \mathrm{IQE}^* = \frac{\mathrm{EQE}}{(1 - R_{\mathrm{meas}})} = \frac{\mathrm{EQE}}{A_{\mathrm{tot}}} = \frac{\mathrm{EQE}}{A_{\mathrm{Sc}} + A_{\mathrm{Pa}}} \tag{3}$$

where R_{meas} is the hemispherical reflectance generally measured with the help of an integrating sphere and A_{Sc} is the absorptance inside the semiconductor. The variable IQE^* was introduced to clearly distinguish between the measurement and the corresponding simulation. It is important to note that this equation only holds if no transmittance through the module occurs. Furthermore, this definition is not equal to the general idea that the IQE describes the share of generated charge carriers inside the semiconductor that contribute to the accessible short-circuit current density J_{sc}

$$\mathrm{IQE}^* \neq \mathrm{IQE} = \frac{\mathrm{EQE}}{A_{\mathrm{Sc}}} = \frac{\mathrm{EQE}}{A_{\mathrm{tot}} - A_{\mathrm{Pa}}}. \tag{4}$$

Rewriting (2) and introducing the angular IQE factor $f_{\mathrm{IQE}}(\theta_i, \lambda)$ and the angular parasitic absorption factor $f_{\mathrm{Pa}}(\theta_i, \lambda)$ allow separating the electrical and the optical change caused by the deviation of the incidence angle from the normal

$$\mathrm{EQE}\left(\theta_i\right) = f_{\mathrm{IQE}} \cdot \mathrm{IQE}_0 \cdot (1 - f_{R,\mathrm{tot}} \cdot R_{\mathrm{tot},0} - f_{\mathrm{Pa}} \cdot A_{\mathrm{Pa},0}) \tag{5}$$

$$f_{\mathrm{IQE}}\left(\theta_i\right) = \frac{\mathrm{IQE}\left(\theta_i\right)}{\mathrm{IQE}_0} \tag{6}$$

$$f_{R,\mathrm{tot}}\left(\theta_i\right) = \frac{R_{\mathrm{tot}}\left(\theta_i\right)}{R_{\mathrm{tot},0}} \tag{7}$$

$$f_{\mathrm{Pa}}\left(\theta_i\right) = \frac{A_{\mathrm{Pa}}\left(\theta_i\right)}{A_{\mathrm{Pa},0}}. \tag{8}$$

The angular correction factors defined above can either be used for a correction procedure, which is presented in Section VII, or if unity is subtracted, it defines the relative change of the corresponding factor compared to the perpendicular case.

For the analysis of the different effects, two different samples were investigated. The first one is a monocrystalline silicon (mono-c-Si) solar cell with a planar damage etched front surface and an aluminum back surface field. This very simple cell type was chosen to reduce the parameters that need to be taken into account and thus be able to effectively separate the angular effects under investigation. The second sample, which was simulated and measured, is a solar module that contains a standard mono-c-Si solar cell onto which a standard texture (KOH etching) is applied. The cell exhibits comparable electrical properties as the planar solar cell, except for the front surface. The sample is referred to as "standard solar module" even though the front side encapsulation is chosen to be a 100 μm polyvinylidene fluoride polymeric film (PVDF) polymeric film produced for solar applications. This choice was made to reduce systematic errors that occur when a thick glass layer is applied to the one cell module sample. The refractive index values that were applied for the simulation of the PVDF and the ethylene-vinyl-acetate (EVA) layer where chosen to be equal to the one of low-iron starphire glass [12] as no specific material data were available.

IV. Angle Dependence of the Reflectance and the Parasitic Absorption

To determine the factors $f_{R,\mathrm{tot}}$ and f_{Pa} for a simple untextured solar cell, an optical model is needed that is capable of describing R, A, and T for different incident angles including

the contact grid and an AR coating on the front side and the contact layer on the backside of the cell. A widely used analytical model is the one introduced by Basore [13], which was later extended by Brendel *et al*. [14]. The model is generally used on the basis of some basic assumptions. First, the first forward and backward passes are assumed to be specular. Second, two different transmission angles are set for the forward and backward pass as a result of a fitting procedure. Third, the light is supposed to be completely diffuse for all of the following transmissions. Fourth, one lumped parameter is assumed for the backside reflectance inside the wafer. As these assumptions obscure the real physical behavior of the solar cell and since no reasonable way to introduce the variation of the AOI was found, we developed a new optical model that meets these limitations by the total separation of the direct and the diffuse paths of the light through the wafer. Furthermore, the contact grid and FCA were integrated into the model as additional elements. The propagation of the specular light was derived using a geometrical series simplification of the form [15]

$$\sum_{k=0}^{\infty} a^k = \frac{1}{1\ -\ a}. \tag{9}$$

The transmission angle θ_t inside the solar cell and thereby the absorption is constant for the forward and backward specular light path at a certain AOI.

In contrast, the diffuse share of the light needs to be described with the help of a double sum series, which is given by the general equation

$$\sum_{k=0}^{\infty}\sum_{n=0}^{k} a^n b^k = \frac{1}{(b\ -\ 1)\,(ab\ -\ 1)}. \tag{10}$$

This representation is needed because the light can be specular for many interactions with the surfaces (inner sum) and suddenly be transformed into diffuse light. As soon as it is diffuse, it stays diffuse until it is either absorbed or it leaves the solar cell (outer sum).

Exemplarily, we show the equation for the overall reflectance R_{tot} where the variables used are depicted in Fig. 1. All of the variables and equations derived for the optical model are presented in Table III in the Appendix

$$\begin{aligned} R_{\mathrm{tot}} &= R_{\mathrm{fe}} + R_{\mathrm{esc,dir}} + R_{\mathrm{esc,diff}} \\ &= R_{\mathrm{fe}} + \frac{T_{\mathrm{fe}}\,(1-h_f)\,(1-h_b)\,T^2 R_b T_f}{1-\ (1-h_f)\,(1-h_b)\,T^2 R_b R_f} \\ &\quad + \frac{T_{\mathrm{fe}}(h_f T_{\mathrm{diff}}^2 R_{b,d} + h_b(1-h_f)T_{\mathrm{diff}} T R_b)T_{f,d}}{\left(T_{\mathrm{diff}}^2 R_{b,d} R_{f,d} - 1\right)\left((1-h_b)\,(1-h_f)\,T^2 R_b R_f - 1\right)}. \end{aligned} \tag{11}$$

The four parameters $R_{b,d},\ R_{f,d},\ h_b$, and h_f have been newly introduced as compared to the traditional models. The first two of these represent the reflectivity of the diffuse radiation when it hits the front or rear side, while the remaining two are the haze factors that indicate how much of the specular light is transferred into diffuse radiation when it intersects with the corresponding surface. It is important to note that these variables represent real physical quantities, which in principle can be measured. However, as the light, which is diffusely reflected, is not purely Lambertian, the diffuse reflection parameters $R_{b,d}$ and $R_{f,d}$ are modified to increase slightly with the AOI. Per degree angle variation, a value of $\mathrm{AOI}/90^\circ \cdot 0.4\%$ is added to the perpendicular value.

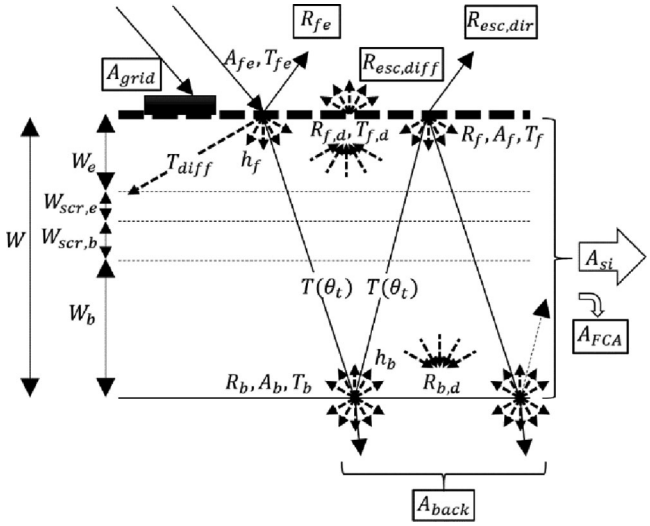

Fig. 1. Illustration of the parameters used for the optical and electrical simulation of an untextured silicon solar cell.

To account for the change in the incidence angle, the absorption coefficients are divided by the cosine of the corresponding angle, which leads to an effective absorption coefficient α'. This also holds true for the FCA. For the diffuse share of light, total Lambertian scattering is assumed, for which the representative angle can be shown to be 60° leading to $\alpha' = \alpha/\cos(60^\circ) = 2\alpha$ [16].

The FCA was modeled using the parametrization proposed in [17], where the FCA for the n-region is given by

$$\alpha_{\mathrm{FCA},n} = 1.68 \cdot 10^{-6} \cdot N_D \cdot \lambda^{2.88} \tag{12}$$

and for the p-region by

$$\alpha_{\mathrm{FCA},p} = 1.8 \cdot 10^{-9} \cdot N_A \cdot \lambda^{1.18} \tag{13}$$

where N_D and N_A are the donor and acceptor densities. For the FCA inside the space charge region (SCR), the absorption coefficient $\alpha_{\mathrm{FCA},n}$ was determined with an assumed carrier density of $N_{D,\mathrm{SCR}} = (N_{D,\mathrm{emitter}} + n_i)/2$, where n_i is the intrinsic carrier concentration.

The contact grid was implemented using the approach in [18] extended by the coverage of the bus bars. The respective shares of the cell, the fingers, and the bus bars are given by M_c, M_{fi}, and M_{bb}.

An untextured mono-c-Si solar cell was simulated and measured for the evaluation of the model. Its cell properties are listed in Table II.

The coating consists of a 86-nm-thick silicon nitride (SiN_x) AR layer and the base diffusion length was set to 200 μm as this

TABLE II
CELL CHARACTERISTICS (L IS THE DIFFUSION LENGTH, S IS THE SURFACE RECOMBINATION VELOCITY, W IS THE TOTAL WIDTH OF THE CELL, AND $M_{\mathrm{bb}}/M_{\mathrm{fi}}/M_c$ IS THE SHARE OF THE BUS BAR, THE FINGER, AND THE SOLAR CELL)

Description	Units	Value
Cell area:	cm²	150
J_{sc}:	mA/cm²	33.65
V_{oc}:	V	0.6
FF:	%	68.37
L_e/L_b:	µm	12/200
S_f/S_r:	cm/s	1e4/800
W:	µm	200
W_e:	µm	0.3
$N_D/\ N_A$:	1/cm³	1e17/1e20
$M_{bb}/M_{fi}/M_c$	%	0/7.73/92.27
h_b/h_f		0.6/0.1
$R_{b,d}/R_{f,d}$		0.81/0.97
Material: SiNx, Si, AlSi, Ag		[20]

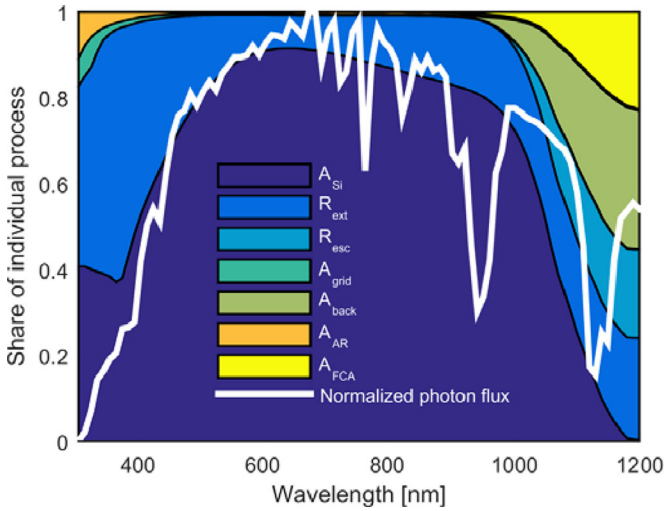

Fig. 2. Share of the absorption and reflection processes of an untextured mono-c-Si cell at perpendicular incidence.

is the approximated value found with the help of the measured IQE by the method described by Spiegel *et al.* [19].

The share of the effects for the simulated untextured mono-c-Si cell at perpendicular incidence is shown in Fig. 2.

In Fig. 3, the accuracy of the simulated reflection in comparison to the measurement values can be seen for the incident angles of 8°, 40°, 60°, and 70°.

The measurement setup for the determination of the angular-dependent reflection consists of a 500 mm diameter integrating sphere with a rotational stage in its center. It was constructed after the principles in [21] and the detector is a silicon photodiode limiting the accuracy for wavelengths <400 nm and >1100 nm. It is important to note that the lowest AOI that is applicable is 8° from the normal. As $R(8°) \approx R(0°)$, we will refer to this as the perpendicular case. Both the measurements and the simulation reveal a strong variation of the reflection curves when the AOI is changed. In addition to this strong angular effect of the reflectivity, the simulation gives the angular results for the parasitic absorption. The corresponding correction factor $f_{\mathrm{PA}} - 1$ is plotted in the upper graph in Fig. 4.

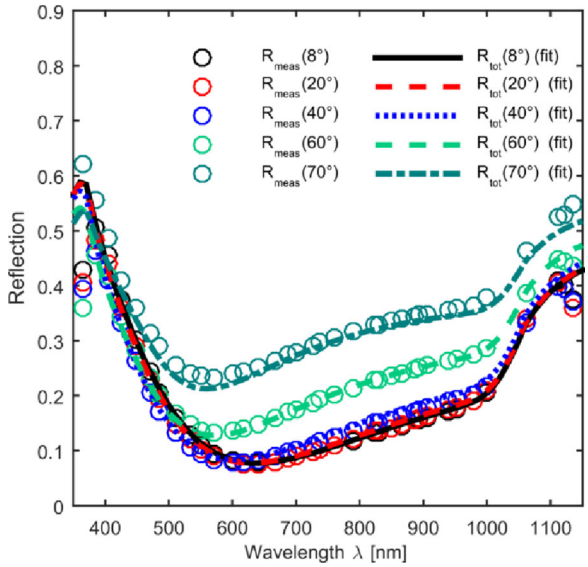

Fig. 3. Comparison of the simulated and the measured reflection curves of an untextured mono-c-Si solar cell.

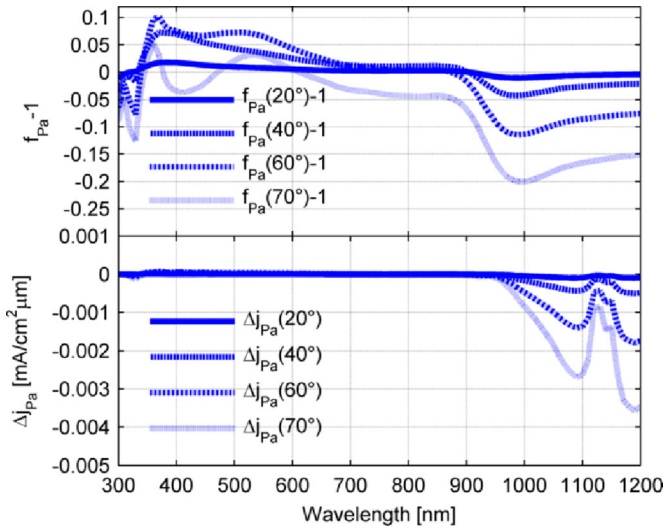

Fig. 4. Correction factor for the parasitic absorption in a planar mono-c-Si cell sample (upper graph) and the corresponding influence on the current density (lower graph).

Even though a strong relative change in the parasitic absorption can be observed for all investigated AOI, the absolute change in the current related to the parasitic absorption is only relevant for wavelengths > 900 nm: This is shown in the lower graph in Fig. 4. The main contribution to this change is due to the increasing backside reflection.

Concerning the optical simulation of textured solar cells, no simple analytical model is available that includes the variation of the AOI. To be capable of determining the angular correction factors for complex module compounds, a modular unit cell

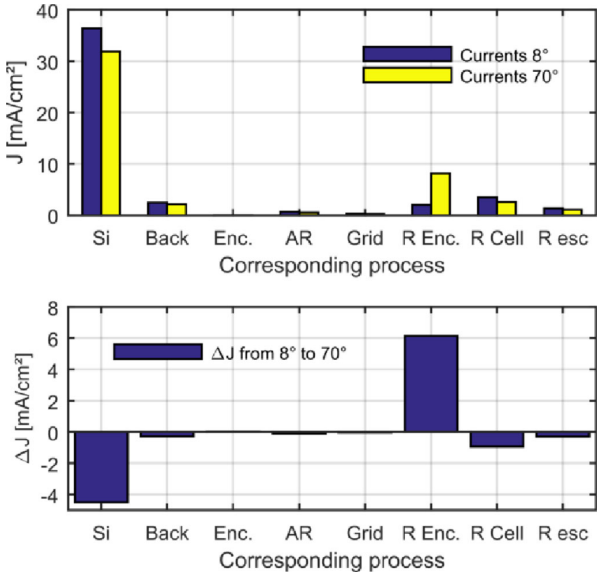

Fig. 5. Current densities of different absorption and reflection channels for a standard module for the incidence angles of 8° and 70° (upper graph) and the absolute difference in current density of the corresponding processes (lower graph).

Monte Carlo ray tracing software was developed. In the software, an arbitrary number of layers can be stacked above each other. The bottom structure of every layer can be determined and it simultaneously defines the top structure of the adjacent layer. At present, upright pyramids and pyramidal grooves with an arbitrary pyramid angle can be chosen. AR coatings can be added at all layer intersections. For the reflection at a material interface, the share of Lambertian scattering can be specified. The generation profile created with the help of the ray tracing software is stored as a function of the effective depth ζ [22], so that it can automatically be used with the scripted PC1D semiconductor simulation software [23]. The ray tracer was extensively tested in comparison to the software Wafer Ray Tracer offered by PV-Lighthouse [24].

To evaluate the effect on the optical performance of the standard solar module under investigation, the absolute changes in current for the incidence angles of 8° and 70° were compared. In the upper graph in Fig. 5, the absolute current densities of the relevant absorption and reflection processes for the two AOI are plotted neglecting the cosine effect. In the lower graph, the absolute change in currents for the corresponding effects is shown.

A very high negative contribution of the reflection at the external encapsulation layer (R enc.) on the total current change can be observed. Positive contributions are seen by the increase of reflectivity on the cell surface and the escape reflection and due to a reduction of the parasitic back surface absorption. The parasitic absorption in the encapsulation layer, the AR coating, and the grid seems to be negligible. But care needs to be taken with the interpretation of these numbers because as fewer photons reach the locations of absorption due to the higher external reflection, the current is reduced from the start. This effect is compensated by a positive angular response of the corresponding processes.

V. Determining the Angular Dependence of the IQE

A model of the electrical transport in the semiconductor is needed to determine $f_{\mathrm{IQE}}(\theta_i, \lambda)$. The one-dimensional generation profile that results from the analytical model described above, which includes the internal reflection and parasitic absorption, is inserted into the continuity equation. Together with the Poisson equation and the transport equations, these form the three basic semiconductor equations. The one-dimensional depletion approximation with a homogeneous emitter doping was applied, and the same approach that Wen *et al*. used for the base current determination was applied to both the emitter and the base in our model [25]. All photons absorbed in the SCR are assumed to be collected due to the high electric field. The total current is then the sum of the current of the three regions emitter, SCR, and base. In each region, two direct light components and two diffuse light components contribute to the current density.

Here, p_{sc} is the share of absorption by the semiconductor without the share of FCA (p_{FCA}). The components $\hat{\phi}$ can be interpreted as the cumulative number of photons emitted from either the top or the bottom surface. The indices a and c indicate the emission of direct and diffuse light from the top surface and the indices b and d indicate the direct and diffuse light from the bottom. The transmission components T in the equations represent the share of the cumulative photon flux that reaches the dedicated region. The upper case plus and minus symbols indicate the forward and backward direction and the indices s and d stand for specular and diffuse light. The parameters η_{forward} and η_{back} are the carrier collection efficiencies for the forward and the backward light flux in the dedicated regions. The corresponding equations are presented in Table IV in the Appendix.

$$\begin{aligned} J_e = p_{\mathrm{sc}} \cdot q \cdot \big(& \hat{\phi}_a \cdot T^{+}_{e,s} \cdot \exp\left(-\left(\alpha' + \alpha'_{\mathrm{FCA},e}\right) W_e\right) \cdot \eta_{\mathrm{back},e} \\ & + \hat{\phi}_b \cdot T^{-}_{e,s} \cdot \exp\left(-\left(\alpha' + \alpha'_{\mathrm{FCA},e}\right) W_e\right) \cdot \eta_{\mathrm{forward},e} \\ & + \hat{\phi}_c \cdot T^{+}_{e,d} \cdot \exp\left(-2\left(\alpha + \alpha_{\mathrm{FCA},e}\right) W_e\right) \cdot \eta_{\mathrm{back},e} \\ & + \hat{\phi}_d \cdot T^{-}_{e,d} \cdot \exp\left(-2\left(\alpha + \alpha_{\mathrm{FCA},e}\right) W_e\right) \cdot \eta_{\mathrm{forward},e} \big) \end{aligned} \tag{14}$$

$$\begin{aligned} J_{\mathrm{scr}} = p_{\mathrm{sc}} \cdot q \cdot \big(& \hat{\phi}_a \cdot T^{+}_{\mathrm{scr},s} \cdot \exp\left(-\left(\alpha' + \alpha'_{\mathrm{FCA,scr}}\right) W_{\mathrm{scr}}\right) \\ & + \hat{\phi}_b \cdot T^{-}_{\mathrm{scr},s} \cdot \exp\left(-\left(\alpha' + \alpha'_{\mathrm{FCA,scr}}\right) W_{\mathrm{scr}}\right) + \hat{\phi}_c \cdot T^{+}_{\mathrm{scr},d} \\ & \cdot \exp\left(-2\left(\alpha + \alpha_{\mathrm{FCA,scr}}\right) W_{\mathrm{scr}}\right) + \hat{\phi}_d \cdot T^{-}_{\mathrm{scr},d} \\ & \cdot \exp\left(-2\left(\alpha + \alpha_{\mathrm{FCA,scr}}\right) W_{\mathrm{scr}}\right) \big) \end{aligned} \tag{15}$$

$$\begin{aligned} J_b = p_{\mathrm{sc}} \cdot q \cdot \big(& \hat{\phi}_a \cdot T^{+}_{b,s} \cdot \exp\left(-\left(\alpha' + \alpha'_{\mathrm{FCA},b}\right) W_b\right) \\ & \cdot \eta_{\mathrm{forward},b} + \hat{\phi}_b \cdot T^{-}_{b,s} \cdot \exp\left(-\left(\alpha' + \alpha'_{\mathrm{FCA},b}\right) W_b\right) \\ & \cdot \eta_{\mathrm{back},b} + \hat{\phi}_c \cdot T^{+}_{b,d} \cdot \exp\left(-2\left(\alpha + \alpha_{\mathrm{FCA},b}\right) W_b\right) \\ & \cdot \eta_{\mathrm{forward},b} + \hat{\phi}_d \cdot T^{-}_{b,d} \cdot \exp\left(-2\left(\alpha + \alpha_{\mathrm{FCA},b}\right) W_b\right) \\ & \cdot \eta_{\mathrm{back},b} \big). \end{aligned} \tag{16}$$

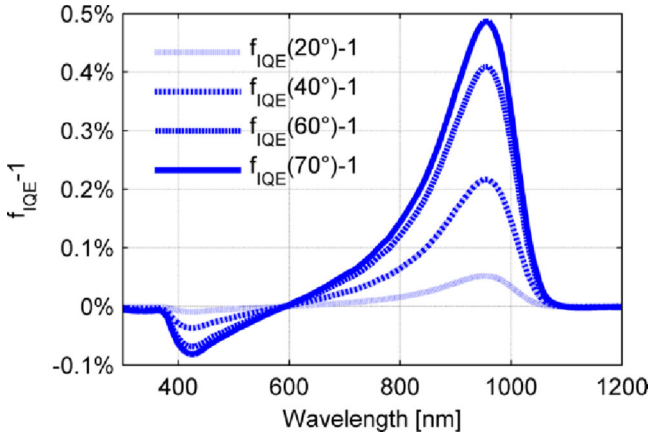

Fig. 6. $f_{\mathrm{IQE}} - 1$ curves of the planar solar cell sample at four different AOI.

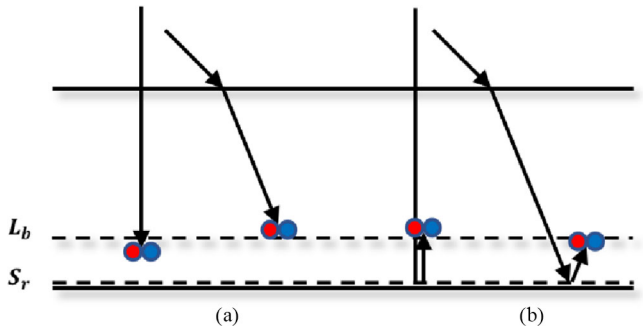

Fig. 7. Illustration of how a tilted pathway creates an electron–hole pair closer or further away from the SCR, compared to the perpendicular case.

The results for the angular correction factor $f_{\mathrm{IQE}} - 1$ of the planar solar cell sample for the incidence angles of 20°, 40°, 50°, and 70° are shown in Fig. 6. A small global minimum can be observed at a wavelength of 420 nm and a much larger global maximum at about 960 nm. Analyzing the origin of the global maximum, two electrical effects were determined that are produced by the change in the AOI.

Both are illustrated in Fig. 7. On the left-hand side an example of how a photon with an oblique trajectory creates an electron/hole pair in the base closer to the SCR than the perpendicular counterpart is shown. At the same time, the charge carrier separation appears further apart from the recombination centers at the backside. Therefore, the charge carriers created by the photons with this specific wavelength will have a higher probability to be collected. This effect is reversed as soon as the photon is reflected at the backside, as depicted in (b). In principle, the same processes appear in the emitter but with the opposite effect.

It is important to note that effect (b) in Fig. 7 is not the reason why the factor $f_{\mathrm{IQE}} - 1$ is reduced to zero at long wavelengths. This is rather due to the fact that the absorption length $1/\alpha$ is much larger than the thickness of the wafer; therefore, the generation profile becomes spatially homogeneous [11], leading to an independence from the AOI.

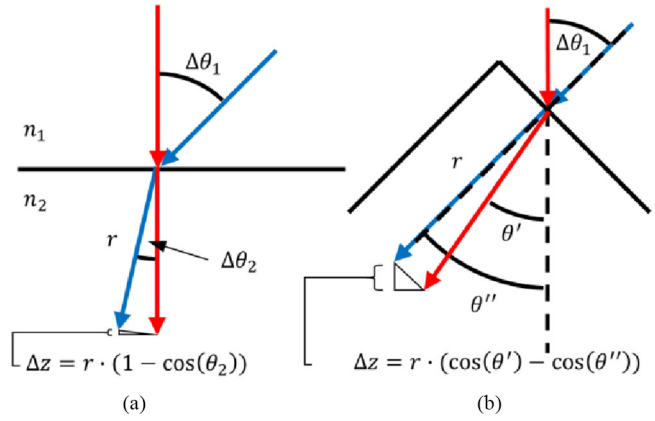

Fig. 8. Schematic representation of the effect that a texture has on the absorption depth reduction Δz in a solar cell.

The effect of the AOI on the IQE is moderate in the planar solar cell sample, but it can be demonstrated that the application of a texture can have a huge impact on the f_{IQE} value. The reason for this is depicted schematically in Fig. 8.

The reduction of the absorption depth Δz is much larger when the light beam inside the wafer is refracted from the start in the case of perpendicular incidence. To account for this effect, we introduce an effective angle that is defined by

$$\theta_{\mathrm{eff}} = p_1 \cdot \theta_1 + p_2 \cdot \theta_2 + \cdots = \sum_{n=1}^{N} p_n \cdot \theta_n \tag{17}$$

where p_n is the share of the light that passes through the wafer at the transmission angle θ_n and N is the number of different paths involved.

Using the ray tracing tool, θ_{eff} was determined for a standard solar module and at a wavelength of 550 nm. The texture was simulated as regular upright pyramids since the random configuration is not yet implemented in the ray tracing tool. The base angle of the pyramids is set to 54.74°. Only those paths were evaluated that occurred directly after the light enters the wafer. Therefore, no internal reflection inside the texture was assumed. The resulting values for θ_{eff} at the AOI from 0° to 80° are presented in Fig. 9.

Two different heuristic fitting functions were found to reproduce θ_{eff} as a function of the AOI. These are given by

$$\theta_{\mathrm{eff}} = \theta_{\mathrm{eff},0} + \frac{\Delta\theta_{\mathrm{eff}}}{2} \cdot \left(1 - \cos\left(\theta_{\mathrm{AOI}} \cdot \frac{\pi}{90^\circ}\right)\right) \tag{18}$$

$$\theta_{\mathrm{eff}} = \theta_{\mathrm{eff},0} + \frac{\Delta\theta_{\mathrm{eff}}}{2} \cdot \left(1 + \mathrm{erf}\left((\theta_{\mathrm{AOI}} - 45^\circ) \cdot \frac{\pi}{90^\circ}\right)\right) \tag{19}$$

where $\theta_{\mathrm{eff},0}$ is the effective angle at perpendicular incidence, which is 38.5° in the case of the standard module and $\Delta\theta_{\mathrm{eff}}$ is the difference between the effective angles at 0° and 90°, which is 9° in the case of the standard module.

These values can now be inserted into the analytical model presented above. Setting the internal front-side reflectance to zero assures that only one forward and one backward pass are simulated. The electrical properties of the implemented mono-c-Si solar cell are comparable to the ones of the planar sample

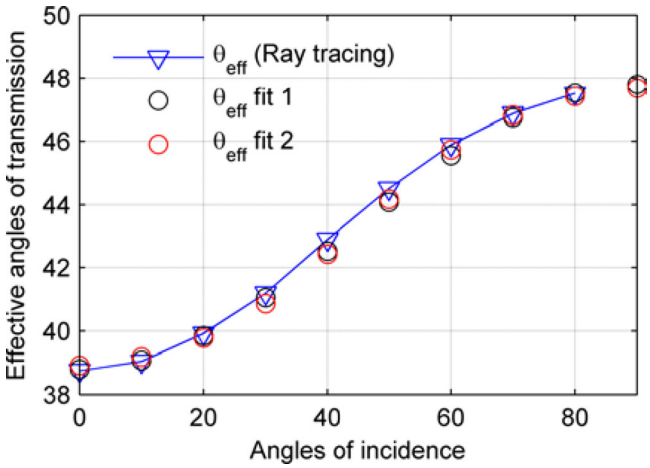

Fig. 9. Effective angles in a standard silicon solar module for all AOI determined by means of ray tracing.

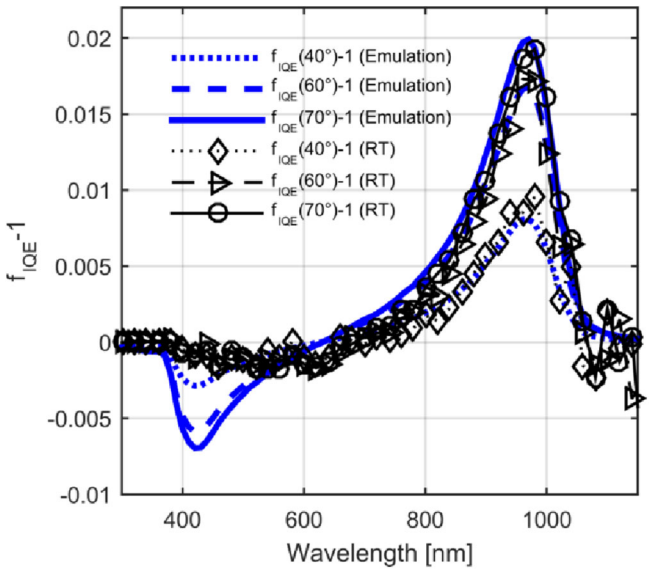

Fig. 10. Comparison of the factor $f_{\mathrm{IQE}} - 1$ of a standard solar module simulated with the help of the effective angle approach and a full ray tracing study for the incidence angles of 40°, 60°, and 70°.

(see Table II). In Fig. 10, the results of this effective angle approach are compared to a ray tracing simulation for the same module type.

The results of the effective angle approach and of the full ray tracing study are in a good agreement for the long wavelength region. The global minimum, which can be observed at about 410 nm in the analytical results, is completely missing in the ray tracing study. This is attributed to the fact that the emitter and the SCR have the same geometric shape as the applied texture, which was solely included into the ray tracing simulation in the form of the effective depth ζ.

It can be seen that the global maximum of $f_{\mathrm{IQE}}(70°) - 1$ is at 2% and is thus four times higher than in the case of the planar solar cell. But the factor f_{IQE} is not only a function of the AOI, but it is also strongly dependent on the cell thickness W, the base

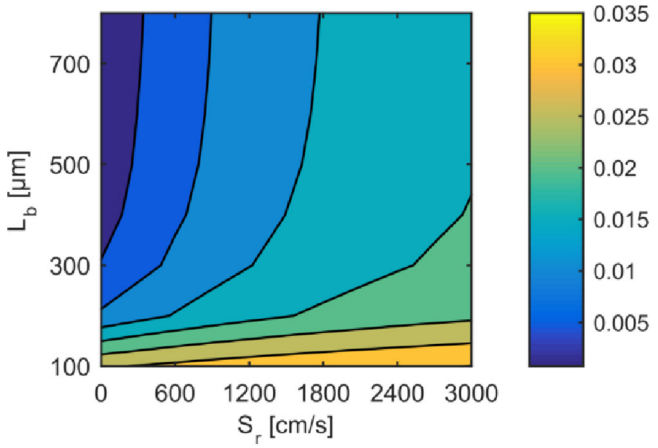

Fig. 11. Contour plot of the global maximum of $f_{\mathrm{IQE}}(70°) - 1$ of a standard solar module as a function of the base diffusion length L_b and the rear surface recombination velocity S_r.

diffusion length L_b, and the rear surface recombination velocity S_r. The dependence of the global maximum of $f_{\mathrm{IQE}}(70°) - 1$ on the parameters L_b and S_r is presented in Fig. 11.

The maximum difference to the IQE at 70° compared to the IQE at perpendicular incidence is larger than 3% for very low diffusion lengths. Here, the influence of S_r is very low, while the surface recombination velocity becomes the dominant factor for high values of L_b.

VI. Measuring the Angle Dependence of the IQE

In this section, the measurement procedure to determine the angular factor $f_{\mathrm{IQE,meas}} - 1$ is described and the results for the planar mono-c-Si cell sample and the standard module are presented and compared to the corresponding simulations of $f_{\mathrm{IQE}^*} - 1$.

The measurement of the IQE at different incident angles is performed in two steps. First, the reflectance is measured with the help of an integrating sphere as described above. Afterward, the spectral response is determined with a measurement setup that consists of a xenon short arc lamp, a filter monochromator equipped with 40 filters, a rotational stage with bias light, and a lock-in amplifier for the noise suppression of the current measurements. The rotation axis of the sample is chosen parallel to the bus bars, so that shadowing by the fingers is avoided.

First, the planar solar cell with the parameters given in Table II was measured at different incident angles and the $f_{\mathrm{IQE,meas}} - 1$ values were subsequently calculated. In Fig. 12, the measured values of $f_{\mathrm{IQE,meas}} - 1$ for the incident angles of 40°, 60°, and 70° (lower graph) are compared to the simulated values of $f_{\mathrm{IQE}^*} - 1$ (upper graph).

The measurement at 70° shows an increase for wavelength values >600 nm, which is comparable to the simulated values. However, the measurement at 60° shows a lower increase than expected. Yet the local maximum at about 950 nm might be caused by the changing IQE. The limited accuracy of the measurement is most probably caused by systematic errors such as

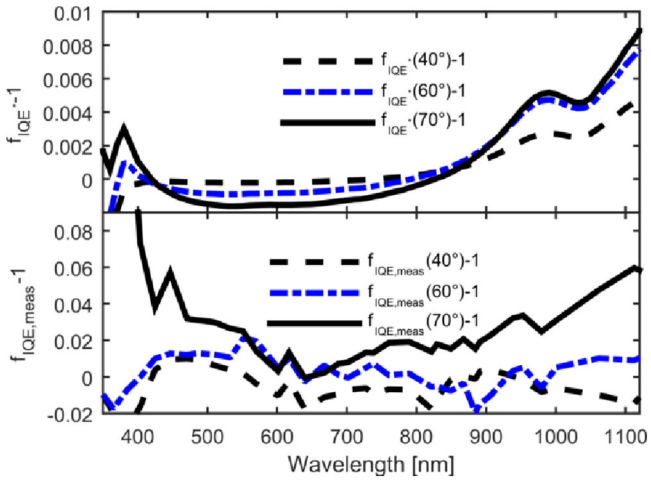

Fig. 12. Simulated values of $f_{\mathrm{IQE}^*} - 1$ of a planar solar cell for 40°, 60°, and 70° (upper graph) in comparison to $f_{\mathrm{IQE,meas}} - 1$ values (bottom graph).

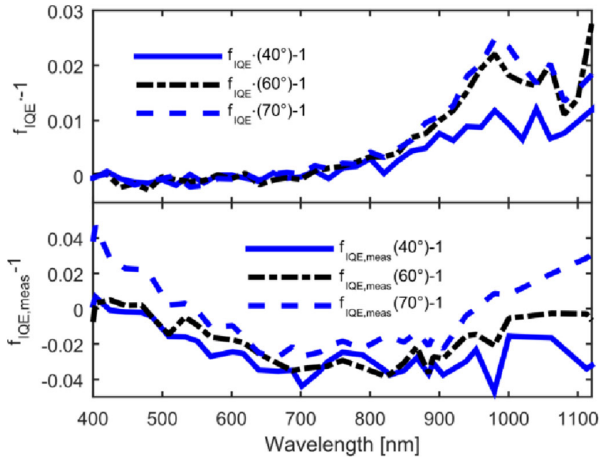

Fig. 13. Simulated values of $f_{\mathrm{IQE}} - 1$ of a standard solar module for 40°, 60°, and 70° (upper graph) in comparison to the measured values (bottom graph).

the light field inhomogeneity, the growing spot size due to the change in the AOI, and hence the influence of the spatial EQE inhomogeneity and the imperfect flatness of the planar cell. The reproducibility, in contrast, is in the range of <0.5% for both measurements. The corresponding EQE curves for the planar cell sample are presented in the Appendix.

Now the results for the standard solar module are presented. In Fig. 13, the measured values for $f_{\mathrm{IQE}^*}(40^\circ) - 1$, $f_{\mathrm{IQE}^*}(60^\circ) - 1$, and $f_{\mathrm{IQE}^*}(70^\circ) - 1$ are compared to the values found with a conducted ray tracing simulation. For the simulation 50 000 rays/λ were traced for wavelengths <960 nm, while 100 000 rays/λ were chosen for longer wavelengths. The share of Lambertian scattering at the backside was selected to be 40% and the rear-side material was chosen to be eutectic AlSi [20].

Here, again the measured values do not exactly fit the simulation, but for all measurements, an increase in the wavelength range between 700 and 1000 nm can be observed, which is comparable to the simulated values.

TABLE III
SUMMARY OF FIVE DIFFERENT MODELS FOR THE CONVERSION OF THE PERPENDICULAR EQE TO THE ANGLE OF INCIDENCE θ_i

	Equations
Model 1	$EQE(\theta_i,\lambda) = EQE_0(\lambda)$
Model 2	$EQE(\theta_i,\lambda) = EQE_0(\lambda) \cdot (1 - R_F(\theta_i))/(1 - R_{F,0})$
Model 3	$EQE(\theta_i,\lambda) = EQE_0(\lambda) \cdot \frac{1 - R_{tot,0}(\lambda) \cdot f_{R,tot}(\theta_i,\lambda)}{1 - R_{tot,0}(\lambda)}$
Model 4	$EQE(\theta_i,\lambda) = EQE_0(\lambda) \cdot \frac{1 - R_{tot,0}(\lambda) \cdot f_{R,tot}(\theta_i,\lambda) - A_{Pa,0}(\lambda) \cdot f_{A,Pa}(\theta_i,\lambda)}{1 - R_{tot,0}(\lambda) - A_{Pa,0}(\lambda)}$
Model 5	$EQE(\theta_i,\lambda) = EQE_0(\lambda) \cdot f_{IQE}(\theta_i,\lambda) \cdot \frac{1 - R_{tot,0}(\lambda) \cdot f_{R,tot}(\theta_i,\lambda) - A_{Pa,0}(\lambda) \cdot f_{A,Pa}(\theta_i,\lambda)}{1 - R_{tot,0}(\lambda) - A_{Pa,0}(\lambda)}$

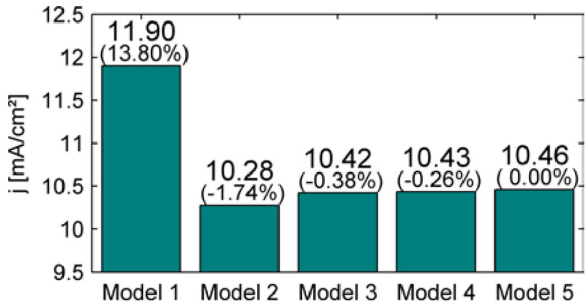

Fig. 14. Results for the current density of a solar standard solar module at 70° AOI calculated by five different models and the corresponding relative deviation from reference model 5.

The reason for the parallel offset of the 40° and 60° curves could not clearly be identified, while the increase for wavelengths <700 nm is attributed to an increase of parasitic absorption in the transparent polymer front-side encapsulation and the applied EVA film, which were emulated with the optical parameters of glass, for the reason of missing optical data of the film and the unknown thickness of the EVA layer.

The measurement results and the corresponding simulations of the EQE and the reflection of the standard solar module sample are presented in the Appendix.

VII. SIGNIFICANCE OF THE ANGULAR CORRECTION FACTORS

To quantify the significance of the different angular effects for the yield prediction, five models for the calculation of the short-circuit current density J_{sc} at an incident angle of 70° were compared. The correction factors used for the models 3–5 were taken from the ray tracing study of the standard solar module presented in the previous section. A standard air mass 1.5 solar spectrum was used as source of radiation.

While in model 1, the EQE is kept at its perpendicular value, the second model uses a Fresnel reflectivity value, which assumes only glass with a refractive index of $n = 1.5$. The correction in model 3 uses the total reflection simulated by means of ray tracing. In model 4, the correction of parasitic absorption is added and model 5 contains the angle dependence of the IQE and thus all described angular correction factors. The results are plotted in Fig. 14.

While models 1 and 2 show a strong deviation from the reference model 5, model 3 gives a result that is much closer. Adding

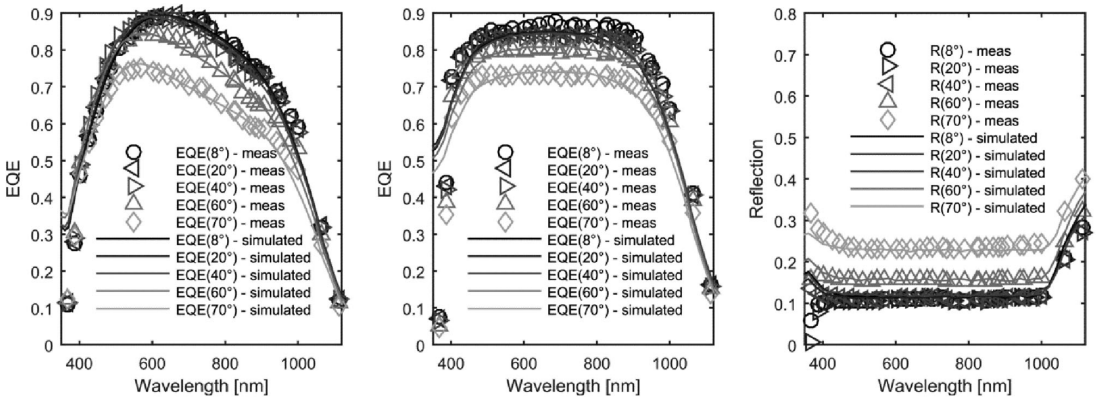

Fig. 15. (Left) Measured and fitted EQE curves of the planar solar cell sample. (Middle) Measured and fitted EQE curves of the standard solar module sample. (Right) Measured and fitted reflection curves of the standard solar module sample.

TABLE IV
COLLECTION OF ALL RELEVANT EQUATIONS OF THE ANALYTICAL SOLAR CELL MODEL

R_{fe}	$R_{fe} = M_{fi} \cdot r_{fi} + M_{bb} \cdot r_{bb} + M_c \cdot r_c$
T_{fe}	$T_{fe} = M_c \cdot t_c$
A_{grid}	$A_{grid} = M_{fi} \cdot a_{fi} + M_{bb} \cdot a_{bb}$
A_{AR}	$A_{AR} = M_c \cdot a_c$
R_b	$R_b = r_b$
R_f	$R_f = (1 - M_c) + M_c \cdot r_f$
T_f	$T_f = 1 - R_f$
$T_{f,d}$	$T_{f,d} = 1 - R_{f,d}$
$r_c/a_c/t_c/r_b$ $/r_f/r_{fi}/a_{fi}$	Calculated with transfer matrix method [26]
T	$T = \exp(-(\alpha + \alpha_{FCA,e}) \cdot W_e/\cos(\theta_t)) \cdot \exp(-(\alpha + \alpha_{FCA,scr}) \cdot W_{scr}/\cos(\theta_t)) \cdot \exp(-(\alpha + \alpha_{FCA,b}) \cdot W_b/\cos(\theta_t))$
T_{diff}	$T_{diff} = \exp(-(2\alpha + 2\alpha_{FCA,e}) \cdot W_e) \cdot \exp(-(2\alpha + 2\alpha_{FCA,scr}) \cdot W_{scr}) \cdot \exp(-(2\alpha + 2\alpha_{FCA,b}) \cdot W_b)$
p_{sc}	$p_{sc} = \alpha \cdot W/(\alpha \cdot W + \alpha_{FCA,e} \cdot W_e + \alpha_{FCA,scr} \cdot W_{scr} + \alpha_{FCA,b} \cdot W_b)$
p_{FCA}	$p_{FCA} = (\alpha_{FCA,e} \cdot W_e + \alpha_{FCA,scr} \cdot W_{scr} + \alpha_{FCA,b} \cdot W_b)/(\alpha \cdot W + \alpha_{FCA,e} \cdot W_e + \alpha_{FCA,scr} \cdot W_{scr} + \alpha_{FCA,b} \cdot W_b)$
A_{tot}	$A_{tot} = A_{dir} + A_{diff}$
A_{dir}	$A_{dir} = \frac{T_{fe}(1-h_f)(1+(1-h_b)TR_b)(1-T)}{1-(1-h_f)(1-h_b)T^2R_bR_f}$
A_{diff}	$A_{diff} = \frac{T_{fe}(h_f+h_b(1-h_f)T_{diff}TR_{f,d}R_b+h_fT_{diff}R_{b,d}+h_b(1-h_f)TR_b)(1-T_{diff})}{(T_{diff}^2R_{b,d}R_{f,d}-1)((1-h_f)(1-h_b)T^2R_bR_f-1)}$
A_{sc}	$A_{sc} = p_{sc} \cdot A_{tot}$
A_{FCA}	$A_{FCA} = p_{FCA} \cdot A_{tot}$
T_{tot}	$T_{tot} = T_{dir} + T_{diff}$
T_{dir}	$T_{dir} = \frac{T_{fe}(1-h_f)T(1-R_b)}{1-(1-h_f)(1-h_b)T^2R_bR_f}$
$T_{diff,tot}$	$T_{diff,tot} = \frac{T_{fe} \cdot (h_f \cdot T(60°) + h_b \cdot (1-h_f) \cdot T(60°)^2 \cdot T \cdot R_{f,d} \cdot R_b) \cdot (1-R_{b,d})}{(T(60°)^2 \cdot R_{b,d} \cdot R_{f,d}-1)((1-h_b)(1-h_f) \cdot T^2 \cdot R_b \cdot R_f-1)}$
$\hat{\phi}_a$	$\hat{\phi}_a = \phi_i \frac{T_{fe}(1-h_f)}{(1-(1-h_f)(1-h_b)T^2R_bR_f)}$
$\hat{\phi}_b$	$\hat{\phi}_b = \phi_i \frac{T_{fe}(1-h_f)(1-h_b)TR_b}{(1-(1-h_f)(1-h_b)T^2R_bR_f)}$
$\hat{\phi}_c$	$\hat{\phi}_c = \phi_i \frac{T_{fe}(h_f+h_b(1-h_f)T_{diff}TR_{f,d}R_b)}{(T_{diff}^2R_{b,d}R_{f,d}-1)((1-h_f)(1-h_b)T^2R_bR_f-1)}$
$\hat{\phi}_d$	$\hat{\phi}_d = \phi_i \frac{T_{fe}(h_fT_{diff}R_{b,d}+d_{rel,b}(1-h_f)TR_b)}{(T_{diff}^2R_{b,d}R_{f,d}-1)((1-h_f)(1-h_b)T^2R_bR_f-1)}$
$T_{e,s}^+ = 1$ $T_{e,s}^- = \exp\left(-\left((\alpha' + \alpha'_{FCA,b}) \cdot W_b + (\alpha' + \alpha'_{FCA,scr}) \cdot W_{scr}\right)\right)$ $T_{e,d}^+ = 1$ $T_{e,d}^- = \exp\left(-2 \cdot \left((\alpha + \alpha_{FCA,b}) \cdot W_b + (\alpha + \alpha_{FCA,scr}) \cdot W_{scr}\right)\right)$	$T_{scr,s}^+ = \exp\left(-(\alpha' + \alpha'_{FCA,e}) \cdot W_e\right)$ $T_{scr,s}^- = \exp\left(-(\alpha' + \alpha'_{FCA,b}) \cdot W_b\right)$ $T_{scr,d}^+ = \exp\left(-2 \cdot \left((\alpha + \alpha_{FCA,e}) \cdot W_e\right)\right)$ $T_{scr,d}^- = \exp\left(-2 \cdot \left((\alpha + \alpha_{FCA,b}) \cdot W_b\right)\right)$	$T_{b,s}^+ = \exp\left(-\left((\alpha' + \alpha'_{FCA,e}) \cdot W_e + (\alpha' + \alpha'_{FCA,scr}) \cdot W_{scr}\right)\right)$ $T_{b,s}^- = 1$ $T_{b,d}^+ = \exp\left(-2 \cdot \left((\alpha + \alpha_{FCA,b}) \cdot W_b + (\alpha + \alpha_{FCA,scr}) \cdot W_{scr}\right)\right)$ $T_{b,d}^- = 1$
$\eta_{forward,e}(\alpha')$	$\eta_{forward,e}(\alpha') = \frac{\alpha' \cdot L_e}{(\alpha'^2 \cdot L_e^2-1) \cdot (1-\exp(-\alpha' \cdot W_e))} \cdot \left(\alpha' \cdot L_e - \frac{\sinh\left(\frac{W_e}{L_e}\right)+\frac{S_n \cdot L_e}{D_e}\cosh\left(\frac{W_e}{L_e}\right)-\left(\frac{S_e \cdot L_e}{D_e}-\alpha' \cdot L_e\right)\exp(-\alpha \cdot W_e)}{\cosh\left(\frac{W_e}{L_e}\right)+\frac{S_e \cdot L_e}{D_e}\cdot\sinh\left(\frac{W_e}{L_e}\right)}\right)$
$\eta_{back,e}(\alpha')$	$\eta_{back,e}(\alpha') = \frac{\alpha' \cdot L_e}{(\alpha'^2 \cdot L_e^2-1) \cdot (1-\exp(-\alpha' \cdot W_e))} \cdot \left(\alpha' \cdot L_e \cdot \exp(-\alpha' \cdot H) - \frac{\left(\sinh\left(\frac{W_e}{L_e}\right)+\frac{S_e \cdot L_e}{D_e}\cosh\left(\frac{W_e}{L_e}\right)\right) \cdot \exp(-\alpha' \cdot W_e)-\left(\frac{S_e \cdot L_e}{D_e}+\alpha' \cdot L_e\right)}{\cosh\left(\frac{W_e}{L_e}\right)+\frac{S_e \cdot L_e}{D_e}\cdot\sinh\left(\frac{W_e}{L_e}\right)}\right)$
$\eta_{forward,b}(\alpha')$	$\eta_{forward,b}(\alpha') = \frac{\alpha' \cdot L_b}{(\alpha'^2 \cdot L_b^2-1) \cdot (1-\exp(-\alpha' \cdot W_b))} \cdot \left(\alpha' \cdot L_n - \frac{\sinh\left(\frac{W_b}{L_b}\right)+\frac{S_b \cdot L_b}{D_b}\cosh\left(\frac{W_b}{L_b}\right)-\left(\frac{S_b \cdot L_b}{D_b}-\alpha' \cdot L_b\right)\exp(-\alpha \cdot W_b)}{\cosh\left(\frac{W_b}{L_b}\right)+\frac{S_b \cdot L_b}{D_b}\cdot\sinh\left(\frac{W_b}{L_b}\right)}\right)$
$\eta_{back,b}(\alpha')$	$\eta_{back,b}(\alpha') = \frac{\alpha' \cdot L_n}{(\alpha'^2 \cdot L_b^2-1) \cdot (1-\exp(-\alpha' \cdot W_b))} \cdot \left(\alpha' \cdot L_b \cdot \exp(-\alpha' \cdot W_b) - \frac{\left(\sinh\left(\frac{W_b}{L_b}\right)+\frac{S_b \cdot L_b}{D_b}\cosh\left(\frac{W_b}{L_b}\right)\right) \cdot \exp(-\alpha' \cdot W_b)-\left(\frac{S_b \cdot L_b}{D_b}+\alpha' \cdot L_b\right)}{\cosh\left(\frac{W_b}{L_b}\right)+\frac{S_b \cdot L_b}{D_b}\cdot\sinh\left(\frac{W_b}{L_b}\right)}\right)$

the parasitic absorption does not make a significant difference to model 3. The effect that the angle dependence of the IQE has on the current density is in the order of –0.26%. However, these values must be taken with caution as they might vary strongly with changing cell technology, module composition, and solar spectrum. Thus, in some cases, the inclusion of some of the angular correction factors might still be relevant for a more precise energy yield prediction.

VIII. Conclusion and Outlook

This work focused on the detailed analysis of angle-dependent effects in silicon solar cells and modules. First, the most important angle-dependent effects were summarized and different angular correction factors were presented that allow the correction of the EQE, the reflection R, the parasitic absorption A_{Pa}, and the IQE from their value at perpendicular incidence to any other AOI. We then presented an optical and electrical model that includes all relevant angle-dependent effects described in Section II. With help of this model, a detailed analysis was conducted for a planar silicon solar cell including the values for $f_{R,\mathrm{tot}}$, $f_{A_{\mathrm{Pa}}}$, and f_{IQE}. The simulation of the planar cell sample showed that the values of f_{IQE} strongly depend on the diffusion length and the surface recombination velocity. Using the same analytical model, the angle dependence of the IQE was emulated for a standard solar module using an effective angle approach. The latter was verified with the help of a ray tracing tool developed for this study.

In the last section, we showed that the increase of the IQE with the change in the incident angle could in principle be seen in the measured samples, though the measurement precision needs to be improved.

An estimation of the significance of the different angle effects showed that the correction of the EQE by an angular correction factor $f_{R,\mathrm{tot}}$ has errors of less than 0.5% for an incident angle of 70° and a spectrum of air mass 1.5.

In subsequent studies, the methodology used in this paper will be applied to modules with a textured front-side encapsulation and other solar cell technologies to analyze their angular characteristics.

Appendix

See Table IV.

References

[1] Measurement of Photovoltaic Current-Voltage Characteristics, 2nd ed., IEC Standard 60904-3, 1989.

[2] M. J. Carvalho, P. Horta, J. F. Mendes, M. C. Pereira, and W. M. Carbajal, "Incidence angle modifiers: A general approach for energy calculations," in *Proc. ISES World Congr.*, 2009, vols. I–V, pp. 608–612.

[3] M. Ebert, H. Stascheit, I. Hädrich, and U. Eitner, "The impact of angular dependent loss measurements on PV module energy yield prediction," in *Proc. 29th Eur. PV Sol. Energy Conf. Exhib.*, Amsterdam, The Netherlands, 2014.

[4] A. Luque Ed., *Handbook of Photovoltaic Science and Engineering*, 2nd ed. Chichester, U.K.: Wiley, 2011.

[5] I. Geisemeyer *et al.*, "Angle dependence of solar cells and modules: The role of cell texturization," *IEEE J. Photovolt.*, vol. 7, no. 1, pp. 19–24, Jan. 2017.

[6] F. Plag, I. Kröger, T. Fey, F. Witt, and S. Winter, "Angular-dependent spectral responsivity-Traceable measurements on optical losses in PV devices," *Prog. Photovolt., Res. Appl.*, vol. 26, no. 8, pp. 565–578, 2017.

[7] J. Nelson, *The Physics of Solar Cells*. London, U.K.: Imperial College Press, 2010.

[8] C. C. Katsidis and D. I. Siapkas, "General transfer-matrix method for optical multilayer systems with coherent, partially coherent, and incoherent interference," *Appl. Opt.*, vol. 41, no. 19, pp. 3978–3987, 2002.

[9] K. R. McIntosh, M. D. Abbott, and B. A. Sudbury, "Ray tracing isotextured solar cells," *Energy Procedia*, vol. 92, pp. 122–129, 2016.

[10] D. Kray, M. Hermle, and S. W. Glunz, "Theory and experiments on the back side reflectance of silicon wafer solar cells," *Prog. Photovolt., Res. Appl.*, vol. 16, no. 1, pp. 1–15, 2008.

[11] R. Brendel, *Thin-Film Crystalline Silicon Solar Cells: Physics and Technology*, 2nd ed. Weinheim, Germany: Wiley-VCH, 2009.

[12] E. Palik, *Handbook of Optical Constants of Solids*, vol. I. Orlando, FL, USA: Academic, 1985.

[13] P. A. Basore, "Extended spectral analysis of internal quantum efficiency," in *Proc. IEEE 23rd Photovolt. Spec. Conf.*, Sep. 1993, pp. 147–152.

[14] R. Brendel, M. Hirsch, R. Plieninger, and J. H. Werner, "Quantum efficiency analysis of thin-layer silicon solar cells with back surface fields and optical confinement," *IEEE Trans. Electron Devices*, vol. 43, no. 7, pp. 1104–1113, Jul. 1996.

[15] M. A. Green, *Silicon Solar Cells Advanced Principles and Practice*. Sydney, N.S.W., Australia: Centre Photovolt. Devices Syst., Univ. New South Wales, 1995.

[16] P. Campbell and M. A. Green, "Light trapping properties of pyramidally textured surfaces," *J. Appl. Phys.*, vol. 62, no. 1, pp. 243–249, 1987.

[17] S. C. Baker-Finch, K. R. McIntosh, D. Yan, K. C. Fong, and T. C. Kho, "Near-infrared free carrier absorption in heavily doped silicon," *J. Appl. Phys.*, vol. 116, no. 6, 2014, Art. no. 63106.

[18] B. Thaidigsmann *et al.*, "Accurate determination of the IQE of screen printed silicon solar cells by accounting for the finite reflectance of metal contacts," in *Proc. Eur. Photovolt. Sol. Energy Conf. Exhib.*, 2009, pp. 2056–2059.

[19] M. Spiegel, B. Fischer, S. Keller, and E. Bucher, "Separation of bulk diffusion length and back surface recombination velocity by improved IQE-analysis," in *Proc. 28th IEEE Photovolt. Spec. Conf.*, Anchorage, AK, USA, Sep. 2000, pp. 311–314.

[20] M. R. Vogt, "Development of physical models for the simulation of optical properties of solar Cell modules," Dissertation, Gottfried Wilhelm Leibniz Univ., Hannover, Germany, 2015.

[21] Standard Test Method for Determining Solar or *Photonic* Reflectance, Transmittance, and Absorptance of Materials Using a Large Diameter Integrating Sphere, ASTM Standard E1175-87, 2015.

[22] S. C. Baker-Finch and K. R. McIntosh, "One-dimensional photogeneration profiles in silicon solar cells with pyramidal texture," *Prog. Photovolt., Res. Appl.*, vol. 20, no. 1, pp. 51–61, 2012.

[23] H. Haug, B. R. Olaisen, Ø. Nordseth, and E. S. Marstein, "A graphical user interface for multivariable analysis of silicon solar cells using scripted PC1D simulations," *Energy Procedia*, vol. 38, pp. 72–79, 2013.

[24] PV Lighthouse, "Wafer ray tracer: PV Lighthouse," 2016.

[25] Z. Wen, W. Wang, C. Zhou, and J. Zhang, "Analytical solution for the photocurrent of solar cells with internal reflection," *J. Appl. Phys.*, vol. 111, no. 3, 2012, Art. no. 34502.

[26] H. A. Macleod, *Thin-Film Optical Filters*, 3rd ed. Bristol, U.K.: Inst. Phys., 2001.

Authors' photographs and biographies not available at the time of publication.